Dependence of electron transfer dynamics on the number of graphene layers in p-stacked 2D materials: insights from ab initio nonadiabatic molecular dynamics†

Hamid Mehdipour,[a] Brendan A. Smith,[b] Ali T. Rezakhani,[a] Saeedeh S. Tafreshi,[c] Nora H. de Leeuw, [iD] [d] Oleg V. Prezhdo, [iD] [e] Alireza Z. Moshfegh [iD] *[af] and Alexey V. Akimov [iD] *[b]

Recent time-resolved transient absorption studies demonstrated that the rate of photoinduced interfacial charge transfer (CT) from Zn-phthalocyanine (ZnPc) to single-layer graphene (SLG) is faster than to double-layer graphene (DLG), in contrast to the expectation from Fermi's golden rule. We present the first time-domain non-adiabatic molecular dynamics (NA-MD) study of the electron injection process from photoexcited ZnPc molecules into SLG and DLG substrates. Our calculations suggest that CT occurs faster in the ZnPc/SLG system than in the ZnPc/DLG system, with 580 fs and 810 fs being the fastest components of the observed CT timescales, respectively. The computed timescales are in close agreement with those reported in the experiment. The computed CT timescales are determined largely by the magnitudes of the non-adiabatic couplings (NAC), which we find to be 4 meV and 2 meV, for the ZnPc/SLG and ZnPc/DLG systems, respectively. The transitions are driven mainly by the ZnPc out-of-plane bending mode at 1100 cm^{-1} and an overtone of fundamental modes in graphene at 2450 cm^{-1}. We find that dephasing occurs on the timescale of 20 fs and is similar in both systems, so decoherence does not notably change the qualitative trends in the CT timescales. We highlight the importance of proper energy level alignment for capturing the qualitative trends in the CT dynamics observed in experiment. In addition, we illustrate several methodological points that are important for accurately modeling nonadiabatic dynamics in the ZnPc/FLG systems, such as the choice of surface hopping methodology, the use of phase corrections, NAC scaling, and the inclusion of Hubbard terms in the density functional and molecular dynamics calculations.

1. Introduction

The design of artificial photovoltaic and photocatalytic materials has been greatly inspired by the chemical and structural features of the known natural photosynthetic complexes. Heteroaromatic metal-containing molecules such as porphyrins are the key functional blocks in the famous Fenna–Mathew–Olson (FMO) complexes.[1] The large molar extinction coefficients[2] of such molecules enables them to efficiently harvest solar photons, while the tunability of their absorption spectrum via functional groups[3] makes possible harvesting photons of different energies. Also, the emergence of long-lived coherences in these materials provides efficient excitation energy transfer pathways in biological complexes.[4] Not surprisingly, heteroaromatic molecules con-taining porphyrin or phthalocyanine motifs are constantly being explored as key candidates for man-made solar energy conversion materials both experimentally[5] and computationally.[6]

Recently, the photo-induced interfacial charge separation in Zn phthalocyanine (ZnPc)/few-layer graphene (FLG) heterojunc-tions has attracted a notable experimental and computational interest.[1–5,7] FLGs are two-dimensional (2D) systems composed of one-atom-thick honeycomb layers of sp^2-hybridized carbon atoms. Such 2D honeycomb layer(s) can be considered one of the carbon allotropes, along with carbon nanotubes, 3D graphene,

[a] Department of Physics, Sharif University of Technology, Tehran, Iran. E-mail: moshfegh@sharif.edu

[b] Department of Chemistry, University at Buffalo, The State University of New York, Buffalo, New York 14260-3000, USA. E-mail: alexeyak@buffalo.edu

[c] Department of Chemistry, Amirkabir University of Technology, Tehran, 15875-4413, Iran

[d] School of Chemistry, Cardiff University, Main Building, Park Place, Cardiff, CF10 3AT, UK

[e] Department of Chemistry, University of Southern California, Los Angeles, California 90089, USA

[f] Institute for Nanoscience and Nanotechnology, Sharif University of Technology, Tehran, Iran

†

and graphite. Among the many new 2D materials, like silicene,[8,9] germanene,[10] or phosphorene,[11] the FLG material has remarkable properties, such as a high electrical conductivity, an unusually large mechanical strength, and a large surface area, which makes it a promising material for optoelectronics[6,12,13] and solar energy conversion.[14–16] ZnPc, a semiconducting metal complex of phthalocyanine, is a promising photosensitizer in photo-voltaic and photo-electrochemical applications since it is both a thermally and chemically stable compound.[17] It is also easily synthesized and is non-toxic to the environment.[2,18]

Graphene's homogenous surface provides the grounds for the large diffusion rate and slow nucleation of thin Pc films. Such surface properties make it possible to form highly crystalline aromatic molecular films on graphene,[19,20] which is advantageous for the fabrication of sensitizer/graphene hybrid photoelectrodes. Such photoelectrodes are component pieces used in photoelectrochemical (PEC) and solar cells. Compounds of phthalocyanine and its metal complexes with graphene[3,4,21,22] and graphene oxides[5,23] have been explored as a photosensitizers in PEC and solar cells. Excellent light-harvesting performance verified by an enhanced photocurrent response and efficient quench of fluorescence of metal Pcs confirm the fast transfer of photo-excited electrons from the aromatic molecules into the FLG substrates.[3–5,21] The fluores-cence quenching of similar Pc/graphene systems indicates that the interaction between the Pc and graphene facilitates the transfer of photo-excited electrons from the Pc to graphene.[1,24–26]

Since the performance of photoanode materials composed of metal-phthalocyanine and FLG in PEC and PV applications is closely related to the dynamics of the photo-excited charges, numerous experiments have been carried out to study such dynamics in these materials.[27,28] Recent research based on optical measurements has revealed that the charge separation in such systems is largely affected by the properties of the FLG, such as the number of graphene layers as well as their stacking arrangement.[27] The charge transfer from ZnPc into FLG is faster into monolayer graphene, whereas surprisingly it is slower into AB-stacked double-layer graphene. These observations reveal that interlayer coupling within the FLG is in a large part responsible for driving hot electrons from the donor molecule to the FLG.[29] In previous studies, approximate approaches have been implemented and used to investigate the effects of the FLG inter-layer coupling on the charge transfer dynamics. These inexpensive approaches evaluate the coupling between electronic states in a way that may erroneously contribute to the charge transfer dynamics. As such, the previous evaluations were limited to being able to only study systems with similar orbital energy differences, and were unable to adequately describe the elastic and inelastic interactions that occur between a quantum electronic subsystem with temperature-dependent atomic vibrations.[30]

We use non-adiabatic molecular dynamics (NA-MD) to study the electron transfer (ET) process from a photoexcited ZnPc into SLG and DLG substrates, and rationalize the counter-intuitive order of rates observed experimentally in these sys-tems as the function of the number of graphene layers.[27] Our study sheds light on the underlying mechanisms of ET in ZnPc/ FLG heterojunctions and factors that determine the ET rates,

such as magnitudes of nonadiabatic couplings (NACs), magnitudes of energy gaps, electronic decoherence, and the nuclear vibrations that drive the electronic transitions. Such knowledge is essential for the rational design of efficient hybrid photoanodes that can effectively separate charge carriers to be used in water splitting processes, namely oxidation of water molecules and subsequent reduction of remained hydrogen ions.[31]

2. Computational methodology

Ground-state optimization, electronic structure calculations, and ground-state molecular dynamics (MD) simulations are performed using PWscf code of the Quantum Espresso package.[32] The valence electrons are described by single electron Kohn–Sham (KS) wave-functions represented in the planewave (PW) basis. The core electrons are described with the norm-conserving pseudo-potentials of Goedecker–Hartwigsen–Hutter.[33] The PW basis size is determined by the electron kinetic energy cut-off of 60 Ry (ca. 800 eV), as determined from our convergence study (Fig. S1 in the ESI†). The electronic exchange and correlation are described within the Perdew–Burke–Ernzerhof (PBE) functional.[34] Semi-empirical DFT-D2 method of Grimme[35] is used to describe the van der Waals interactions between the adsorbed molecule and graphene layer(s). The atomic forces needed in MD are computed using a relatively dense 3 3 1 Monkhorst–Pack k-point mesh, which can accurately represent the Brillouin zone (BZ). A denser 8

8 1 Monkhorst–Pack k-point mesh is used to compute partial densities of states at the optimized interface structure and at several structures randomly selected from the MD steps at 300 K. In order to perform the expensive calculation of the nonadiabatic couplings (NACs), we use energy eigenvalues and wave functions calculated at the G-point. The use of multiple k-points is critical for obtaining more accurate forces, whereas the KS orbitals and their energies are less sensitive to the selection of k-point mesh in this system, which may be partially attributed to its relatively large size.

An orthorhombic supercell of the dimensions a = 16.76 and b = 17.04 Å is used to model the ZnPc/SLG and ZnPc/DLG interfaces (Fig. 1). We utilize the atomistic setups previously used by Biancardi et al.[29] In these simulation cells, the ZnPc molecule covers the FLG surface almost completely, which mimics the thin film geometry used in the experiment.[27,36] For both interfaces, a vacuum of 20 Å in the c direction is set to avoid artificial interactions between the interface and its periodic replica in this direction. The size and coordinates of the optimized interfaces obtained with the above computational methodologies are summarized in Tables S2 and S3 of ESI.†

The optimized geometries are then verified by density of states calculations to see if the electronic structures of the graphene(s), ZnPc, and the combined systems agree with the broadly accepted electronic structures for such systems. The optimized structures are then thermalized to room temperature (RT, 300 K) using Born–Oppenheimer molecular dynamics coupled to an Anderson thermostat with the characteristic system-bath (thermostat inertia) time of 8 fs for a time duration over 1 ps. This stage of the simulation protocol is intended to sample initial conditions for
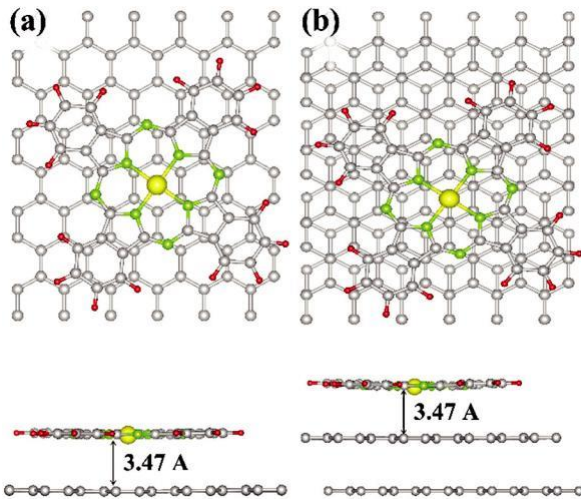
Fig. 1 Optimized geometries of the ZnPc/SLG (a) and ZnPc/DLG (b) interfaces. Top and bottom panels are the plane and side views of the relaxed structures, respectively. C, Zn, N, and H atoms are represented by gray, yellow, green, and red-colored balls, respectively. Here, the energy cutoff is 60 Ry, and a 3 3 1 Monkhorst–Pack mesh is used. The Hubbard parameters of U = 7.0 eV for the Zn atom and U = 5.5 eV for the C and N atoms are used.

modeling NA-MD. The thermalized structures are used as the starting points for the 4 ps ground electronic state adiabatic MD integrated using Verlet algorithm with an integration time step of 1 fs to sample trajectories from the NVE ensemble. These trajectories are then used to perform surface hopping NA-MD calculations.

The charge transfer (CT) dynamics from ZnPc molecule into FLG substrates is computed using the NA-MD methodology formulated within the neglect of back-reaction approximation (NBRA).[37] The development branch of the Libra code[37] is utilized to perform all NA-MD calculations. Within the NA-MD framework used, the time-evolving wavefunction of the system, $C(r,t)$, is represented in the basis of functions, $F_i(r;R(t))$, para-meterized by the time-dependent nuclear trajectories, $R(t)$:

$$C(r, t) = \sum_i c_i(t) F_i(r; R(t)). \quad (1)$$

Furthermore, the NBRA implies that the nuclear dynamics is propagated on a single electronic state, which in this study is taken to be the ground electronic state. Such an approximation is primarily motivated by the excessive computational cost of the direct excited-state-specific nuclear dynamics prescribed by Tully's original surface hopping method.[38] The use of the NBRA is justified by the general ''rigidity'' of the studied system, in which no significant distortions, such as bond breaking or isomerization, are expected to occur on the excited state. To assess the validity of this assumption, we have compared the geometries of the system optimized in its ground and excited state of interest. The excited state in this test is modeled with the DSCF methodology (Section S2 of the ESI†). We find that the two geometries are very close to each other, which suggests that the NBRA dynamics is likely to be close to the rightful TSH dynamics. The use of the NBRA may potentially affect the

results in the following way: because of the non-zero difference in the ground and excited state forces (which is zero by definition in the NBRA), decoherence in the original TSH approach would be faster. As demonstrated recently by two of us, faster decoherence leads to faster charge transfer.[39] Therefore, the use of the NBRA may potentially underestimate the computed CT rates.

The basis functions, $\{F_i(r;R(t))\}$, are chosen as Slater determinants (SDs) constructed from 1-electron orbitals, $\{f_i\}$:

$$F_i = \frac{1}{\sqrt{N}} \det f_{i_1} f_{i_2} \ldots f_{i_N}.$$ In the present work, the orbitals are chosen as the eigenfunctions of the Kohn–Sham (KS) Hamiltonian, parametrically-dependent on time through nuclear geometry:

$$H_{el}^{KS}(R(t))f_i(r;R(t)) = e_i(R(t))f_i(r;R(t)). \quad (2)$$

Following an earlier formulation, the energies of states F_i, E_i, are given by the sums of the corresponding 1-electron energies plus a correction (as will be discussed later).

The time-evolution of the overall wavefunction, $C(r,t)$, is dictated by the time-dependent Schrodinger equation (TD-SE), which translates into a set of differential equations for state amplitudes, $\{c_i(t)\}$:

$$i\hbar \frac{dc_i}{dt} = \sum_j \left(E_i d_{ij} - i\hbar d_{ij} \right) c_j. \quad (3)$$

Here, d_{ij} is the time-derivative NAC, $d_{ij} = \left\langle F_i \left| \frac{\partial}{\partial t} \right| F_j \right\rangle$. In our implementation, it is computed using the numerical approach of Hammes–Schiffer and Tully.[40] As has been pointed out recently,[41] the basis functions for NA-MD (dynamical basis) computed at consecutive timesteps, e.g. at times t and t + Dt, may be inconsistent in their phases. As such, we utilize a suitable phase correction approach[41] to fix any phase inconsistencies before computing NACs. In addition, we keep track of the identity of the dynamical basis states over the MD trajectories to determine and fix potential occurrences of trivial crossings. For the latter we, use the ''mincost'' algorithm of Nelson et al.[42] In our implementation, the state identities are first tracked over the entire duration of the MD trajectory. If the identity of the states is changed at any point over the duration of the MD trajectory, the states are reordered according to the original ordering, to ensure that the original order is preserved. This may mean that the energy of a state ''1'' may be higher than the energy of a state ''2''.

The evolution of state amplitudes, $\{c_i(t)\}$ in eqn (1), is used to compute instantaneous state transition probabilities. The latter is then used to compute the statistics of the trajectory branching, which yields the time-dependent populations of all states. In this work, we utilize the fewest switches surface hopping (FSSH) method of Tully,[38] as well as the decoherence-induced surface hopping (DISH) method of Jaeger et al.[43] DISH accounts for electronic decoherence in the quantum system interacting with the environment, and has been applied for a broad range of organic, inorganic, etc. compound materials.[30,44–47] The DISH calculations require the pure dephasing times for all pairs of states. In the Libra implementation used in this work, they are computed directly from the thermally averaged fluctuations of

the corresponding energy gaps,[48] as can be derived from the optical response theory.[49]

In computing NACs, we first consider 11 (for SLG) and 16 (for DLG) KS orbitals with energies above and below the Fermi energy. A subset of these KS orbitals is used to construct the dynamical bases of SDs to model CT dynamics in ZnPc/FLG systems (Fig. 2). In particular, the donor (starting) states are chosen to be ZnPc-localized excitations (Fig. 2, EX boxes), which are constructed as the intra-ZnPc electron transitions (e.g. HOMO 2 - LUMO+2 or HOMO 2 - LUMO+3 for ZnPc/ SLG or HOMO 4 - LUMO+2 or HOMO 4 - LUMO+3 for ZnPc/DLG). The acceptor (final) states are chosen to be ZnPc - FLG states (Fig. 2, CT boxes), which are constructed as the electronic transitions between orbitals localized on different components of the system (e.g. HOMO 2 - LUMO or HOMO 2 - LUMO+1 for ZnPc/SLG system). In our NA-MD calculations, we first compute the time-dependent (via TSH) population dynamics of all SD states, starting from any of the two SDs in the ''EX'' group. Since the objective is to study the rate of charge transfer, we track the total population of all the SDs in the ''CT'' group, since all of them correspond to the charge-separated state.

The KS orbitals computed along the 4 ps of the ground-state MD trajectory are used to compute NACs in the SD basis, generating 4000 data points, each of which corresponds to a unique MD steps. Following the approach of Prezhdo and co-workers,[50,51] we generate longer (8000 data points) time-series of effective Hamiltonians by duplicating the original 4000 points and concatenating the original set with its replica. Out of the resulting set of 8000 points, the 20 equally distant points (covering the 1 ps interval) are considered the starting points of the NA-MD trajectories. This scheme allows to further extend the sampling of nuclear trajectories, practically at no additional cost. The remaining data points, as well as the part of the initial 1000 data points, are used to define the time-series of Hamiltonians used in the NBRA-NA-MD calculations. We select to run 4 ps-long NA-MD trajectories. The TD-SE, eqn (3), is integrated along each of the 20 sub-trajectories to produce 20 histories of coherent evolution, $\{c^{n}_{i}(t), n = 1, . . ., 20\}$. Larger numbers of configurations do not make much change in the dynamics (Fig. S3, ESI†). In order to sample the statistics of the electronic surface hops,

1000 realizations of the stochastic TSH process is used for each nuclear trajectory. Thus, our approach utilizes the double sampling strategy, which sums to 20 000 surface hopping trajectories in total. We find such a total to sufficiently provide a statistically meaningful description of electronic transitions dynamics.

The time-dependent population of all CT-type states is described by:

$$P(t) = 1.0 \quad (a \quad e^{t/t_e} + b \quad e^{(t/t_g)^2}), \qquad (4)$$

where, t_e and t_g are the time constant for the exponential and Gaussian growth laws, respectively, and a and b are the corresponding weights. The Gaussian component accounts for the initial dynamics, stemming from the coherent transitions (Gaussian and cosine have similar asymptotics), while the exponential component accounts for the incoherent transitions. In fact, the DISH-based calculations employ only the exponential fitting (b = 0).

Detailed scripts and input files used for all types of calculations are available at https://github.com/AkimovLab/Project_ZnPc_few_layer_graphene.

3. Results and discussion

3.1. Structure and molecular dynamics of ZnPc/FLG interfaces

Our calculations indicate the choice of the computational method with properly converged parameters is critical to obtaining reasonable geometries of the optimized structures. For example, using a pure DFT functional such as PBE and kinetic energy cutoff below 50 Ry, a distorted graphene structure (see Fig. 3a) is found to be the most stable, at odds with expectations of planar geometry of the interface. The planarity is only achieved when the electronic on-site Coulomb terms are added via the DFT+U method with U = 7 eV added for Zn atom and U = 5.5 eV added for C and N atoms and the cutoff energies are above the 50 Ry (Fig. 3c and Fig. S4, ESI†). Our calculations of the FLG yield the planar structures even when the PBE functional is used. At the same time, using PBE with low kinetic energy cutoff (below 50 Ry) and without +U correction yields a distorted ZnPc/SLG structure. Using a relatively high kinetic energy cutoff value with the bare PBE functional results in a distorted ZnPc/SLG structure (Fig. S4, ESI†). On the contrary, PBE+U calculations yield planar graphene (within the heterostructure) even at relatively low kinetic energy cutoff values. Therefore, we conclude that the distortion of graphene within the heterostructure is caused mainly by the improper treatment of electronic exchange within the ZnPc molecule at the PBE level.

The planar geometry of the ZnPc/FLG systems has been reported in the previous theoretical works,[29,52] which employed DFT with a range-separated hybrid functional, which would account for the effects we describe above. In the present work, the DFT+U approach is chosen for MD simulations because it delivers the best compromise between the accuracy of hybrid functionals and the computational efficiency of pure functionals (which exhibit very poor scaling in the PW-based implementations). Also, the use of DFT+U results in a high quality prediction of
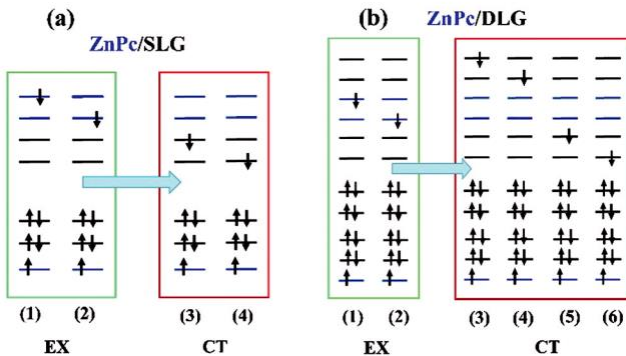

Fig. 2 Dynamical bases used to model CT dynamics in (a) ZnPc/SLG and (b) ZnPc/DLG systems.
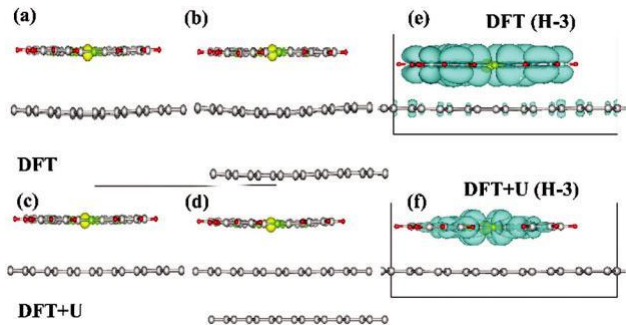
Fig. 3 The role of computational methodology in defining the structures and charge density of the ZnPc/FLG systems. (a and c) ZnPc/SLG and (b and d) ZnPc/DLG structures optimized using PBE (a and b) and PBE+U (c and d) methods. Here, the energy cutoff is 60 Ry, and a 3 3 1 Monkhorst–Pack mesh is used. The values of the Hubbard correction are U = 7.0 eV for the Zn atom and U = 5.5 eV for both the C and N atoms. The small rippling observed in PBE calculations (a and b) disappears when the Hubbard correction is employed (c and d). The C, Zn, N, and H atoms are represented by the gray, yellow, green, and red-colored balls, respectively. The bare PBE calculations yield overly delocalized ZnPc orbitals (e), which also extend into SLG. The PBE+U calculations (f) yield localized ZnPc orbitals in the center of the ZnPc moiety.
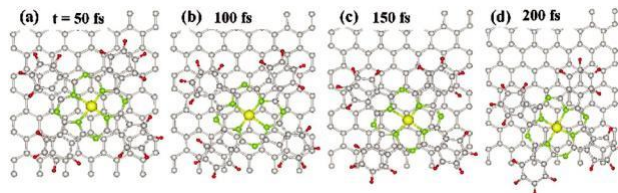

Fig. 4 Geometries of the ZnPc/SLG interface at different times after the interface is thermalized to room temperature: (a)–(d) are snapshots of the relative orientations of the ZnPc molecule with respect to SLG at times 50, 100, 150, and 200 fs. Gray, yellow, green, and red balls represent C, Zn, N, and H atoms, respectively. Here, the energy cutoff is 60 Ry, and a Monkhorst–Pack mesh of 3 3 1 is used. The values of the Hubbard correction are U = 7.0 eV for the Zn atom and U = 5.5 eV for the C and N atoms.

other properties such as (a) the calculated distance of 3.47 Å separating the ZnPc molecule from the graphene surface and (b) the adsorption energy of ca. 2.0 eV. Both parameters are con-sistent with the values reported previously by Duverger et al.[52] The earlier work of Biancardi et al.[29] suggests that the ZnPc/ FLG heterostructure interface has a near planar geometry. Such calculations were performed using a hybrid DFT method, which can account for the above-mentioned discrepancy in the exchange interactions but is not affordable for MD calculations. The use of the Hubbard on-site correction is helpful in this regard. As our calculations suggest, the PBE+U functional yields the nearly planar geometry of the interface, consistent with the geometry of Biancardi et al.[29] Furthermore, by exploring various types of such corrections (Fig. S5, ESI†), we find that corrections on both Zn and C atoms are needed. We find that the correction on N atom orbitals are not essential, likely due to small number of N atoms in the systems. When the Hubbard correction is added to only the Zn atoms leads, a slightly distorted structure is observed following geometry optimization (Fig. S5a, ESI†). The planarity of graphene is restored when we use U = 5.5 eV for the C atoms (Fig. S5c and d, ESI†). Although it is unconventional to use DFT+U with the +U correction on C atoms, we note that a number of other authors have utilized such an approach[53,54] to obtain the bandgap energy and lattice constants closer to those values measured experimentally. These works suggest that the Hubbard correction on non-metal atoms was needed for obtaining accurate structural parameters.

The emergence of rippling in the FLG structures can be explained by noting that there is a lack of long-range exchange in the PBE functional that results in excessive electron delocalization, a well-known and appreciated problem of pure density functionals.[55] The extended range of Zn d-electrons (Fig. 3e) leads to an increased repulsion from the graphene p-electrons. The FLG distortion

(Fig. 3a and b) is therefore a direct consequence of such electronic interactions. The use of the Hubbard correction on the Zn atom facilitates the electron localization within the ZnPc moiety. With this correction, the ZnPc electrons are no longer overly extended into the FLG (Fig. 3f) and no longer cause the significant additional repulsion. In addition, their enhanced localization in the center of ZnPc unit enables enhanced polarizability of the central region, leading to stronger dispersion interactions, which attracts Zn to the FLG substrate and enabling the planar structure.

The earlier computational study of Biancardi et al.[29] employed static zero-temperature calculations to explore the electronic couplings in ZnPc/FLG systems and thus focused on three energetically-favorable orientations of ZnPc with respect to FLG substrates. The present work explores the dynamics of the heterostructure at RT through a direct ab initio constant-temperature MD simulation. As pointed out in the experimental work of Wang et al.,[36] the orientation of the planar molecule on FLG substrate does not affect the rate of CT at the molecule/FLG interface. In present work, we start from a single arbitrary orientation (Fig. 1), which then explores various regions of configurational space (Fig. 4). The long distance separating ZnPc from FLG indicates that the two components interact via non-covalent p-type interactions (Fig. 1). ZnPc and FLG have distinct in-plane symmetries and are thus incommensurate. As a result, they cannot maintain their relative positions under RT condition, see Fig. 4.

3.2. Electronic structure of ZnPc/FLG interfaces

Projected densities of states (pDOS) for FLG and ZnPc moieties in the combined system are displayed in Fig. 5. For both SLG and DLG, the DOS projected onto the FLG component exhibits zero gaps (but practically no states at Fermi level), similar to that of the total DOS of pristine SLG computed elsewhere.[29,56] Using the PBE functional, a bandgap of 1.7 eV is calculated for ZnPc molecule, which is close to 2.0 eV energy gap obtained by Amin et al.[57] and Biancardi et al.[29] using hybrid functionals, and to that measured experimentally.[29,58] According to Fermi's Golden Rule (FGR), the ET rates are proportional to the density of acceptor states at the energy of the donor state. Applied to the present system, the LUMO and LUMO+1 states of ZnPc act
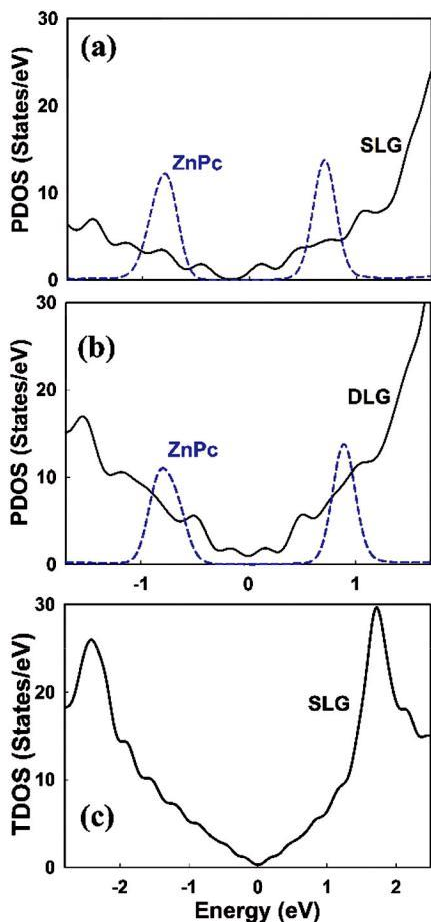
Fig. 5 Densities of electronic states projected onto SLG/DLG (black solid) and ZnPc (blue dashed) fragments in the optimized ZnPc/SLG (a) and ZnPc/DLG (b) heterostructures. The Fermi energy is set at zero for both systems. (c) A reference DOS of a single graphene layer. All DOS have been computed with the energy cut-off of 80 Ry and 8 8 1 Monkhorst–Pack k-point mesh. Also, the value of the Hubbard correction is U = 7.0 eV for the Zn atom and U = 5.5 eV for the C and N atoms.

couplings between AB-stacked DLG and ZnPc are smaller than the couplings between SLG and ZnPc moieties due to wavefunction interference and delocalization effects in the DLG. However, this work relied on a static picture, in which only several configurations corresponding to local energetic minima have been considered. As our MD calculations suggest, the system can explore many more configurations (Fig. 4), whereas the high-symmetry configurations may not be the only ones that determine the ET rates.

The analysis of electronic structure suggests that the ZnPc molecule has two energetically close lowest unoccupied orbitals (with energies 1.78 and 1.72 eV) located 0.83 eV above the Fermi level of ZnPc/FLG heterojunction. These states are LUMO+2 and LUMO+3 in the total set of KS orbitals of the ZnPc/SLG system. A close inspection of the states' identities reveals that they may experience trivial crossings along the MD trajectory (Fig. S6, ESI†). Such crossings are facilitated by the ZnPc symmetry that makes the two orbitals energetically close. Analogously, SLG orbitals (LUMO and LUMO+1) also experience infrequent trivial crossings, also due to high symmetry of the SLG substrate allowing for multiple energetically-close orbitals. For the ZnPc/DLG system, the ZnPc-localized orbitals correspond to LUMO+4 and LUMO+5 of the entire system with the energies of 0.65 and 0.7 eV (above Fermi level), respectively (Fig. S7, ESI†).

In the present work, the excited states of the ZnPc/FLG systems are modeled with the computationally-affordable 1-electron KS orbitals picture, which lacks many-body effects. As a result, the energies of the ZnPc-localized excitons are predicted to be too high in energy (0.65–0.83 eV), which is inconsistent with the ultraviolet photoelectron spectroscopy (UPS) measurements[36] and many-body electronic structure calculations[27] Such references suggest the ZnPc excitons lie only 0.3–0.4 eV above the Fermi energy in both ZnPc/SLG and ZnPc/DLG systems. To account for this discrepancy of 1-electron KS orbital description of excited states in modeling their dynamics, we shift the energies of ZnPc excitations down as detailed in Fig. S8 (ESI†).

The utilized KS-DFT approach to modeling dynamics of the excited states is known to be simplistic. In addition to the intrinsic deficiencies of DFT in describing excited states (even within the TD-DFT formulation), the employed 1-electron orbital picture is missing the many-body effects in describing the excited states' energies and wavefunctions. On the other hand, the conceptually sound approaches such as direct TD-DFT calcula-tions are prohibitively expensive for the present periodic systems. For this reason, we resort to using empirical corrections of the energy levels, by shifting the computed KS-based energies to match the values obtained from the UPS measurements. Such a
correction of energy levels has been employed previously in other works.[59–61]

As has been demonstrated earlier,[55] the NACs between pairs of states are closely related to the corresponding energy gaps. Therefore, if the energies of the states are shifted, the NACs must be rescaled according to the ratio of original and corrected energy gaps to reflect the corresponding energy renormalization. In this way, the empirical correction we employ affects not only the energies but also the couplings used in the NA-MD simulations.

as the donor states. The electron is injected from the ZnPc states into the manifold of the FLG conduction states at that energy and then can further relax to lower FLG conduction states non-radiatively. Our calculations show that the DOS in SLG (Fig. 5a) at the energy of ZnPc donor states is smaller than in DLG (Fig. 5b). This is because of the presence of a second graphene layer in DLG, which contributes more C 2p-states to the pDOS.

Based on a simple FGR argument, one would expect larger ET rates into DLG than into SLG. In contrast to this intuitive expectation, the experimentally-determined ET rates into AB-stacked DLG (the DLG considered in the present work) are smaller than ET rates for SLG.[27] However, the simplest form of FGR assumes that the couplings between the donor and any of the involved acceptor states are equal to each other. In reality, the couplings between different pairs of states may be distinct, even if the acceptor states are energetically close. The electron coupling argument has been supported previously by the work of Biancardi et al.[29] The authors showed that the electronic

In this work, we rescale NACs between ZnPc and SLG or DLG states as exemplified in Section S6 of the ESI.† Note, that NACs among the ZnPc or among the FLG only states are left unchanged since the energy levels within these subsets remain fixed. The shifts in state energies do not qualitatively affect the energy levels alignment in the ZnPc/SLG system, but does reduce the number of potential acceptor states in the ZnPc/DLG system by moving the ZnPc exciton levels below a pair of nearly-degenerate DLG states (Fig. S8, ESI†).

3.3. CT dynamics in the ZnPc/FLG interfaces

To model the ET dynamics in ZnPc/FLG systems, we construct a minimalistic model with the states essential to the process of interest, selected based on the pDOS calculations and comparison with the UPS measurements.[36] Fig. 6 illustrates the KS orbitals and their relative energies (adjusted to the experimental data) included in our model. The excited states of ZnPc are formed by promoting electrons to the ZnPc-localized unoccupied orbitals, LUMO+2, and LUMO+3 for both ZnPc/SLG and ZnPc/DLG systems. One can notice a slight delocalization of LUMO+2 onto SLG, which is an indication of a stronger electronic coupling between ZnPc and SLG than of ZnPc and DLG. The ZnPc-localized states can then decay nonadiabatically to the lower-energy states. The latter are localized on the SLG or DLG (Fig. 6). Thus, the non-adiabatic non-radiative relaxation corresponds to interfacial ET.

Since only a single monolayer of ZnPc on FLG surfaces is considered in this work, the higher energy excitations are notably separate from the lowest ones (e.g. observe the isolated, relatively narrow bands of ZnPc states, Fig. 5), which may be understood even from the particle-in-a-box perspective. Because of the high energy separation, the hot excited states are unlikely to contribute significantly to CT dynamics in single-layer ZnPc/FLG systems. As

the thickness of ZnPc film increases, the excited states may form a wider band, such that hot excitons and hot charge carriers are expected to contribute more to the overall CT process. However, the increased thickness of ZnPc may facilitate exciton diffusion in the ZnPc film away from the interface, thus reducing the CT rates in such systems.[36]

The results of our dynamical calculations in the two systems are summarized in Fig. 7 and Table 1. The curves show the evolution of the total population of all CT-type configurations (red boxes in Fig. 2). The first row in Fig. 7 illustrates the ET dynamics computed using the FSSH technique, whereas the second row corresponds to the dynamics computed using DISH method that accounts for decoherence effects. We observe that CT occurs on the order of 0.52 ps (FSSH, PC = 1, Gaussian) in ZnPc/SLG and 1.0 ps (FSSH, PC = 1, exponential) in ZnPc/DLG, almost twice slower than in the former system. Although these numbers are somewhat larger than those inferred from the time-resolved spectroscopy measurement,[27] our qualitative prediction agrees with the experiment – the CT proceeds faster

Fig. 7 The dynamics of electron injection from the ZnPc molecule to the FLG systems obtained using SH and DISH models and accounting for phase correction: the curves show the total population of the ET states in ZnPc/SLG (solid curves) and ZnPc/DLG (dotted curves) interfaces. PC = 1 and 0 denote ET dynamics with and without the implementation of the phase correction of the adiabatic states.
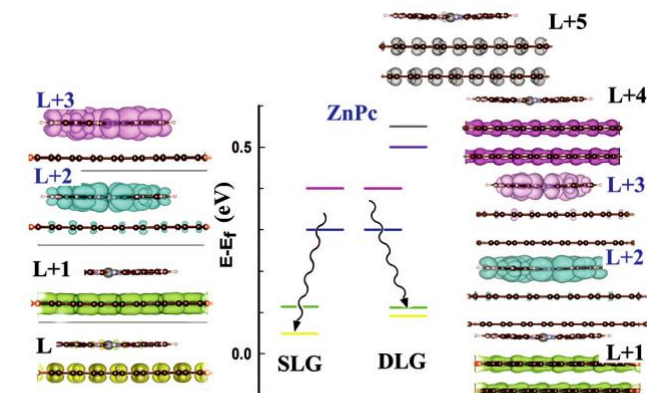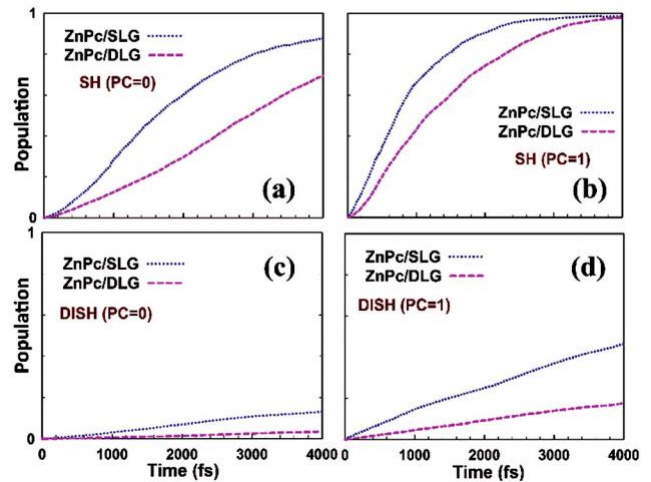

Fig. 6 A schematic showing orbital characters and their relative energies. Only the conduction band orbitals necessary to modeling ET in the ZnPc/SLG and ZnPc/DLG systems are shown. The charge distributions of the KS orbitals are shown in the order of increasing energy. The KS energy levels are corrected to match the UPS measurements (see Section S7 of the ESI†). Here, the energy cutoff is 80 Ry, and an 8 8 1 Monkhorst–Pack mesh is used. Also, the value of the Hubbard corrections are U = 7.0 eV for the Zn atom and U = 5.5 eV for the C and N atoms.

Table 1 The time constants and their weights obtained from fitting the time-dependent population of all CT-type configurations to the function, $P(t) = a\,\exp^{-\frac{t}{t_{e}}} + b\,\exp^{-\frac{t^2}{t_{g2}}}$, for various modeling procedures (FSSH and DISH/mSDM; with phase correction (PC = 1) or not (PC = 0))

Timescales, ps	FSSH (PC = 0)	DISH (PC = 0)	FSSH (PC = 1)	DISH(mSDM) (PC = 1)
ZnPc/SLG				
t_e	2.50 a = 0.58	33.26 a = 1.00	1.11 a = 0.42	10.00 a = 1.00
t_g	1.48 b = 0.41	—	0.52 b = 0.58	—
ZnPc/DLG				
t_e	8.48 a = 0.49	118.62 a = 1.00	1.0 a = 0.36	18.35 a = 1.00
t_g	2.12 b = 0.50	—	1.35 b = 0.64	—

in ZnPc/SLG system than in ZnPc/DLG, even though the former system has the lower density of acceptor states than the latter. Here we compared the shortest timescales in the fitting: inter-estingly, CT in ZnPc/SLG is dominated by Gaussian kinetics, whereas CT in ZnPc/DLG is dominated by exponential kinetics. The exponential timescales, which determine the long-time kinetics, are essentially similar in the two systems.

The discrepancy between the computed and measured time-scales may be attributed to the use of computationally-affordable G-point calculations. Ideally, one may need to consider CT occurring at multiple k-points. As a result, the total density of acceptor states would be scaled up for both systems, leading to an increase in the overall rates. However, such a scaling is expected to affect both systems in a similar way. Thus, we suspect that including multiple K-points is likely to change only the absolute values, but not the trends.

As expected, the inclusion of decoherence makes the CT dynamics follow exponential decay kinetics, removing the Gaussian component. It also significantly slows down the ET dynamics, although notably beyond the experimentally-measured timescales. In this case, DISH (with phase correction, PC = 1) predicts CT timescales of 10 ps for ZnPc/SLG and 18.35 ps for ZnPc/DLG. With decoherence, the ratio of the timescales in ZnPc/SLG and ZnPc/DLG, becomes close to 1 : 2. This is similar to the ratio of the fastest CT components in the FSSH dynamics, but is different from the approximate 1 : 1 ratio of the exponential decay timescales. Thus, decoherence does not change the "observed" order of the time-scales, but it affects the mechanisms leading to these ratios.

This disagreement of DISH calculations with experimental values may originate from the way decoherence is included in this model. In DISH, the transitions aren't attempted before the "decoherence event" is encountered. The rate of such events occurring is determined by the dephasing times. In the case of extra-long dephasing times (highly-coherent), the coherence is maintained for a long time, and surface hopping does not occur. As a consequence, the presence of notably-long dephasing (vide infra) effectively shuts down the transitions in the DISH calculations.

Finally, it is illustrative to discuss the role of the phase-correction (PC, right panels in Fig. 7, PC = 1 in Table 1). Overall, it accelerates the dynamics in all systems but does not lead to qualitative changes in the order of ET rates. The acceleration of the dynamics due to accounting for PC may be quite significant: if in FSSH calculations on ZnPc/SLG it reduces the timescales by 2.5–3 times, the exponential timescales in FSSH calculations on ZnPc/DLG with and without PC vary by 8.5 times. Such scaling factors are much more notable when decoherence corrections are included. In this case, it may be a matter of 18 ps vs. 119 ps (e.g. DISH for ZnPc/DLG, Table 1). Thus, we conclude that PC is critical for obtaining more accurate results.

To assess the uncertainties in computed dynamics, all the calculations are repeated five times using the same setting (Fig. S10, ESI†). We observe only negligible variation in the computed time-dependent populations from one NA-MD run to another, suggesting very small error associated with the NA-MD calculations.
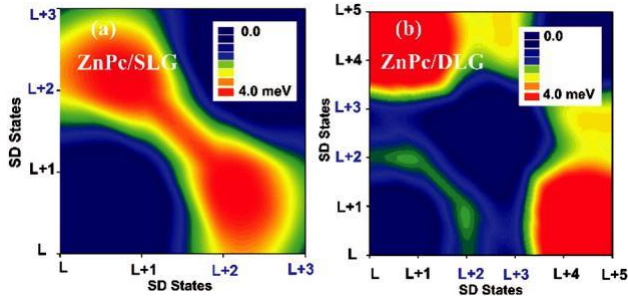

Fig. 8 Contour plot of time-averaged non-adiabatic coupling (NAC) between electronic states. The black and blue colored orbital indexes denote ES and TS states (initial excitation in ZnPc and transferred electron states in FLG), respectively. The very large NACs between SD states related to a transition within a pair of states within FLG or ZnPc have been set to zero in.

The observed trends in the computed CT timescales can be attributed to the relative magnitudes of NACs between donor and acceptor states as well as to the dephasing times. The NAC map showing the couplings between all of the involved states in the two systems studied is depicted in Fig. 8 (the effect of PC is illustrated in Fig. S11 and S12, ESI†). The numerical values of the time-averaged NAC magnitudes are also summarized in Table 2. One can see that in the ZnPc/SLG system, the donor states (overall LUMO+2 and LUMO+3) are strongly coupled to the acceptor (LUMO and LUMO+1) states, with NACs on the order of 4 meV (Table 2). On the contrary, in the ZnPc/DLG system, the couplings are twice as small, with a value of 2 meV. This ratio of NACs translates into a similar ratio of the fastest FSSH timescales. This is because only the FSSH rates without decoherence do not scale quadratically with the NAC magnitude, as one would expect from FGR standpoint.[62] When decoherence is included, the scaling becomes quadratic, such that the 2-fold increase in NAC of ZnPc/SLG in comparison to ZnPc/DLG should translate into a 4-fold acceleration of CT dynamics. However, we observe only a 2-fold increase in the rates. This is because the density of states in ZnPc/DLG is also twice larger than that in ZnPc/SLG. The upper levels of DLG are only slightly above the donor states of ZnPc (Fig. S8 and S9, ESI†), so they can be populated. However, they are strongly coupled to lower DLG states (e.g., see Fig. 8b), which results in fast electron thermalization.

Table 2 (and Fig. S11 and S12, ESI†) also illustrates the mechanism by which PC affects the dynamics. As one may expect, this occurs mainly via modification of average NACs. We observe that in all systems, PC always leads to larger NACs. This effect is likely system-specific, as PC is also known to have the opposite effect of making average NACs smaller.

Table 2 Time-averaged non-adiabatic coupling (NAC) in meV averaged for all pairs of states in active space for ZnPc/SLG and ZnPc/DLG systems computed with (PC = 1) and without (PC = 0) phase-correction

	PC=0	PC=1	PC = 0[a]	PC = 1[a]
ZnPc/SLG	2.31	2.80	3.07	4.23
ZnPc/DLG	1.24	1.49	1.47	2.00

[a] NACs between ZnPc's L and FLG's L+1 states.

To understand the mechanism of CT deceleration by deco-herence, we have analyzed the ensemble-averaged dephasing times. We find they are similar for both systems: 22 fs for ZnPc/ SLG and 19 ZnPc/DLG. As explained above, in DISH, the state transition is decided only at the end of coherence intervals. This means the timescales predicted by DISH would need to be scaled by the dephasing times,[43,62] which should yield approxi-mately 20-fold deceleration of the dynamics. This is consistent with the 10–20-fold increase of the CT timescales observed in our calculations. Since the dephasing times in both systems are similar, the decoherence does not change the qualitative trends in the computed timescales.

To understand the similarity of the dephasing in the two systems and also to characterize the electron–phonon inter-actions that are responsible for interfacial CT, we compute the ACF of the energy gap fluctuations for both systems (Fig. 9a) and their Fourier transformations (influence spectrum, Fig. 9b). The computed ACF and influence spectra of the two systems show no notable distinctions. The influence spectrum shows that the CT is driven by the 1100 cm^{-1} phonon, which corresponds to the out-of-plane bending B_{2g} mode of ZnPc.[63] A very small peak at around 2450 cm^{-1} can be attributed to an overtone of the lower fundamental modes of graphene.[64,65] Two intense phonon modes

at B20 and 70 cm^{-1} are predicted theoretically by previous works.[66] We believe that the presence of only a few phonon modes being coupled to the donor and acceptor states is a significant reason behind the persistent oscillations of the ACF and the relatively long dephasing times.

Finally, we explore the role of the energy levels alignment. In particular, we use the orbitals' order obtained directly from DFT calculations and are not corrected to match the UPS measurements. In this case, we only explore the dynamics computed with FSSH method. As Fig. S13 (ESI†) illustrates, the order of the computed timescales is reversed with respect to that computed with the energy levels shifted and corresponding NAC rescaling. Such calculations are also inconsistent with the experi-mental trends. The rationale for this effect is the following. As one can observe (Fig. S9, ESI†), the energy gap between the original ZnPc levels and the closest FLG levels is larger in ZnPc/ SLG than in ZnPc/DLG. Correspondingly, the unscaled NACs are smaller in the ZnPc/SLG system, leading to slower dynamics in this system, which is in contrast to experimental observations. The coupling to the higher-energy states of DLG leads to the inevitable relaxation of an injected electron to the lower-energy states of DLG, since the magnitude of NACs between DLG levels is large (Fig. 8b). Thus, we conclude that correcting the band alignment consistent with UPS measurements and the corres-ponding NAC rescaling are critical to constructing a real-time dynamics model that can explain the experimental observations. Although such empirical corrections are not generally desirable, they seem unavoidable in modeling nonadiabatic dynamics complex systems like ZnPc/FLG at this point. However, the corrections do not have to be based on experimental data, as more sophisticated and accurate computational methods become feasible.

4. Conclusions

In this work, we study CT dynamics in ZnPc/SLG and ZnPc/DLG p-stacked 2D systems. Stimulated by the time-resolved spectro-scopy measurements of Wang et al.[27] who found a counter-intuitive order of CT rates in these systems and the static electronic structure calculations of Biancardi et al.[29] who proposed an explana-tion based on electronic (diabatic) couplings, we have undertaken real-time DFT-based non-adiabatic molecular dynamics calculations.

We observe faster CT in the ZnPc/SLG system than in the ZnPc/DLG system, but only when the donor energy levels are corrected to match UPS spectra and the corresponding NACs are rescaled proportionally to the changes of energy gaps. We find that the FSSH methodology yields time-averaged CT timescales of 580 fs and 810 fs for ZnPc/SLG and ZnPc/DLG, respectively, which is within the same order of magnitude reported in the experiment. We attribute discrepancies to the absence of a multiple k-points descrip-tion of the manifold of the acceptor states in our model. We show that including phase corrections in the NA-MD methodology is important since it accelerates the dynamics, bringing the computed timescales (above) in closer agreement with experiment. Without such correction, the timescales may be larger by a factor of 2–8.
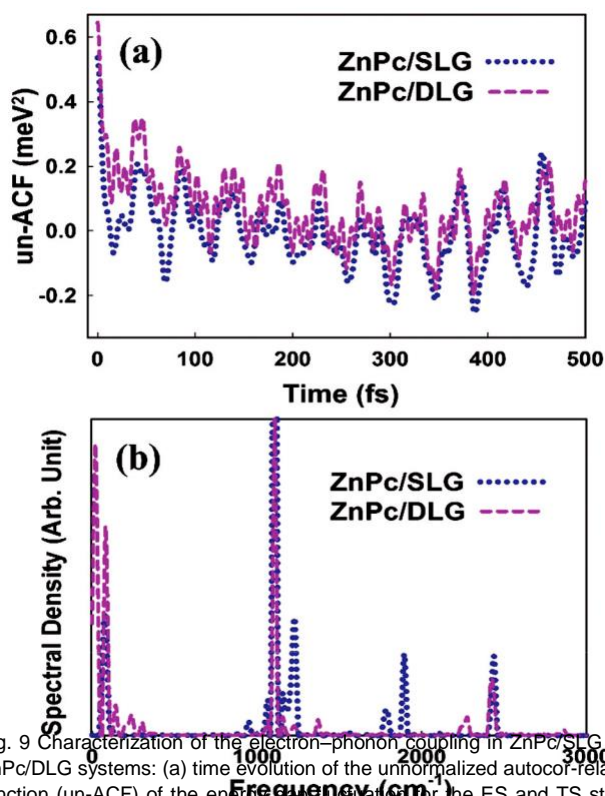

Fig. 9 Characterization of the electron–phonon coupling in ZnPc/SLG and ZnPc/DLG systems: (a) time evolution of the unnormalized autocor-relation function (un-ACF) of the energy gap fluctuation for the ES and TS states contributing in electron transfer in ZnPc/SLG (dotted) and ZnPc/ DLG (dashed curve); (b) phonon influence spectrum contributing into the ET process across the ZnPc/SLG (dotted) and the ZnPc/DLG (dashed curve) interfaces.

We find that the ordering of the CT timescales in the two systems is dictated mainly by the differences in the NAC magnitudes, which correlates with the explanation of Biancardi et al. We find that time-averaged NACs that determine CT in ZnPc/SLG and ZnPc/DLG are 4 meV and 2 meV, respectively. The time-averaged NACs depend on the phase correction in NA-MD calculations. The NAC ratio trans-lates into the ratio of fastest CT rates (FSSH) or to the ratio of the exponential decay rates (DISH) in these systems.

We find that accounting of decoherence effects (via DISH) does not change the qualitative trends in the CT timescales. The computed dephasing times, ca. 20 fs, are similar for the two systems, and thus a comparable deceleration is observed between the systems when decoherence effects are included. In treating for decoherence effects, we find that DISH overestimates the CT rates by a factor of 10, which can be attributed either to the method's limitation or to the way in which decoherence occurs in real systems as opposed to ZnPc/FLG models used. We find that the dephasing can be attributed to a few phonon modes that are coupled to the donor and acceptor states. In particular, we identify phonon modes at $B20$ and 70 cm^{1}, 1100 cm^{1} (out-of-plane bending B_{2g} ZnPc), and 2450 cm^{1} (overtone of lower fundamental modes of graphene) are the main drivers of the CT in both systems.

In passing, we would like to clarify that despite providing some qualitative insights into the charge transfer dynamics in ZnPc/FLG systems, the present work should be regarded only as a zeroth-order approximation to modeling NA-MD. The important effects stemming from a multiconfigurational treatment of ZnPc excited states, accounting for multiple k-points in the graphene subsystems (which may open up more channels for CT), incorporat-ing electron-nuclear back-reaction during excited states dynamics, and better approaches to decoherence may be needed for a more definitive description of the photophysics in the studied ZnPc/FLG interfaces. The present results should be re-evaluated with more accurate methods in the future when they become available.

Conflicts of interest

There are no conflicts to declare.

Acknowledgements

Notes and references

1 C. B. Kc, G. N. Lim and F. D'Souza, Angew. Chem., Int. Ed., 2015, 54, 5088–5092.

2 G. Bottari, M. A. Herranz, L. Wibmer, M. Volland, L. Rodrıguez-Pe´rez, D. M. Guldi, A. Hirsch, N. Martı´n, F. D'Souza and T. Torres, Chem. Soc. Rev., 2017, 46, 4464–4500.

3 D. Wang, J. Huang, X. Li, P. Yang, Y. Du, C. M. Goh and C. Lu, J. Mater. Chem. A, 2015, 3, 4195–4202.

4 D. Akyu¨z, B. Keskin, U. -Sahintu¨rk and A. Koca, Appl. Catal., B, 2016, 188, 217–226.

5 J. Huang, Y. Wu, D. Wang, Y. Ma, Z. Yue, Y. Lu, M. Zhang, Z. Zhang and P. Yang, ACS Appl. Mater. Interfaces, 2015, 7, 3732–3741.

6 G. Haider, R. Ravindranath, T.-P. Chen, P. Roy, P. K. Roy, S.-Y. Cai, H.-T. Chang and Y.-F. Chen, Nat. Commun., 2017, 8, 256.

7 P. A. Troshin, R. Koeppe, A. S. Peregudov, S. M. Peregudova, M. Egginger, R. N. Lyubovskaya and N. S. Sariciftci, Chem. Mater., 2007, 19, 5363–5372.

8 C. Chowdhury and A. Datta, J. Phys. Chem. Lett., 2017, 8, 2909–2916.

9 D. Jose and A. Datta, Acc. Chem. Res., 2014, 47, 593–602.

10 A. Nijamudheen and A. V. Akimov, J. Phys. Chem. C, 2017, 121, 6520–6532.

11 R. Long, W. Fang and A. V. Akimov, J. Phys. Chem. Lett., 2016, 7, 653–659.

12 H. A. Hafez, S. Kovalev, J.-C. Deinert, Z. Mics, B. Green, N. Awari, M. Chen, S. Germanskiy, U. Lehnert, J. Teichert, Z. Wang, K.-J. Tielrooij, Z. Liu, Z. Chen, A. Narita, K. Mu¨llen, M. Bonn, M. Gensch and D. Turchinovich, Nature, 2018, 561, 507–511.

13 P. Alonso-Gonza´lez, A. Y. Nikitin, F. Golmar, A. Centeno, A. Pesquera, S. Ve´lez, J. Chen, G. Navickaite, F. Koppens, A. Zurutuza, F. Casanova, L. E. Hueso and R. Hillenbrand, Science, 2014, 344, 1369–1373.

14 R. Won, Nat. Photonics, 2010, 4, 411.

15 H. Fei, J. Dong, M. J. Arellano-Jime´nez, G. Ye, N. Dong Kim, E. L. G. Samuel, Z. Peng, Z. Zhu, F. Qin, J. Bao, M. J. Yacaman, P. M. Ajayan, D. Chen and J. M. Tour, Nat. Commun., 2015, 6, 8668.

16 D. Mateo, I. Esteve-Adell, J. Albero, J. F. S. Royo, A. Primo and H. Garcia, Nat. Commun., 2016, 7, 11819.

17 C. Ingrosso, A. Petrella, P. Cosma, M. L. Curri, M. Striccoli and A. Agostiano, J. Phys. Chem. B, 2006, 110, 24424–24432.

18 D. Jancˇula and B. Marsˇ´alek, Chemosphere, 2012, 88, 962–965.

19 A. J. Marsden, L. A. Rochford, D. Wood, A. J. Ramadan, Z. P. L. Laker, T. S. Jones and N. R. Wilson, Adv. Funct. Mater., 2016, 26, 1188–1196.

20 M. Bazarnik, J. Brede, R. Decker and R. Wiesendanger, ACS Nano, 2013, 7, 11341–11349.

21 N. Karousis, J. Ortiz, K. Ohkubo, T. Hasobe, S. Fukuzumi, A. Sastre-Santos and N. Tagmatarchis, J. Phys. Chem. C, 2012, 116, 20564–20573.

22 J.-M. Wang, Z.-K. Wang, M. Li, C.-C. Zhang, L.-L. Jiang, K.-H. Hu, Q.-Q. Ye and L.-S. Liao, Adv. Energy Mater., 2018, 8, 1701688.

23 H. Wu, Z. Chen, J. Zhang, F. Wu, F. Xiao, S. Du, C. He, Y. Wu and Z. Ren, Small, 2018, 14, 1702896.

24 K. C. C. Bikram, S. K. Das, K. Ohkubo, S. Fukuzumi and F. D'Souza, Chem. Commun., 2012, 48, 11859–11861.

25 L. Brinkhaus, G. Katsukis, J. Malig, R. D. Costa, M. Garcia-Iglesias, P. Va´zquez, T. Torres and D. M. Guldi, Small, 2013, 9, 2348–2357.

26 L. Zhang, W. Wang, S. Sun, Y. Sun, E. Gao and J. Xu, Appl. Catal., B, 2013, 132–133, 315–320.

27 T. Wang, Q. Liu, C. Caraiani, Y. Zhang, J. Wu and W.-L. Chan, Phys. Rev. Appl., 2015, 4, 014016.

28 S. M. Aly, M. R. Parida, E. Alarousu and O. F. Mohammed, Chem. Commun., 2014, 50, 10452.

29 A. Biancardi, C. Caraiani, W.-L. Chan and M. Caricato, Phys. Chem. Lett., 2017, 8, 1365–1370.

30 A. V. Akimov, A. J. Neukirch and O. V. Prezhdo, Chem. Rev., 2013, 113, 4496–4565.

31 M. Faraji, M. Yousefi, S. Yousefzadeh, M. Zirak, N. Naseri, T. H. Jeon, W. Choi and A. Z. Moshfegh, Energy Environ. Sci., 2019, 12, 59–95.

32 P. Giannozzi, et al., J. Phys.: Condens. Matter, 2009, 21, 395502.

33 C. Hartwigsen, S. Goedecker and J. Hutter, Phys. Rev. B: Condens. Matter Mater. Phys., 1998, 58, 3641–3662.

34 J. P. Perdew, J. A. Chevary, S. H. Vosko, K. A. Jackson, M. R. Pederson, D. J. Singh and C. Fiolhais, Phys. Rev. B: Condens. Matter Mater. Phys., 1992, 46, 6671–6687.

35 S. Grimme, J. Comput. Chem., 2006, 27, 1787–1799.

36 T. Wang, T. R. Kafle, B. Kattel, Q. Liu, J. Wu and W. L. Chan, Sci. Rep., 2016, 6, 28895.

37 A. V. Akimov, J. Comput. Chem., 2016, 37, 1626–1649.

38 J. C. Tully, J. Chem. Phys., 1990, 93, 1061.

39 B. Smith and A. V. Akimov, J. Chem. Phys., 2019, 151, 124107.

40 S. Hammes-Schiffer and J. C. Tully, J. Chem. Phys., 1994, 101, 4657.

41 A. V. Akimov, J. Phys. Chem. Lett., 2018, 9, 6096–6102.

42 S. Fernandez-Alberti, A. E. Roitberg, T. Nelson and S. Tretiak, J. Chem. Phys., 2012, 137, 014512.

43 H. M. Jaeger, S. Fischer and O. V. Prezhdo, J. Chem. Phys., 2012, 137, 22A545.

44 A. V. Akimov, J. T. Muckerman and O. V. Prezhdo, J. Am. Chem. Soc., 2013, 135, 8682–8691.

45 Z. Zhou, J. Liu, R. Long, L. Li, L. Guo and O. V. Prezhdo, J. Am. Chem. Soc., 2017, 139, 6707–6717.

46 R. Long and O. V. Prezhdo, ACS Nano, 2015, 9, 11143–11155.

47 R. Long and O. V. Prezhdo, Nano Lett., 2015, 15, 4274–4281.

48 A. V. Akimov and O. V. Prezhdo, J. Phys. Chem. Lett., 2013, 4, 3857–3864.

49 S. Mukamel, Principles of Nonlinear Optical Spectroscopy, 1999.

50 J. Jankowska and O. V. Prezhdo, J. Phys. Chem. Lett., 2017, 8, 812–818.

51 H. Mehdipour, A. V. Akimov, J. Jankowska, A. T. Rezakhanai, S. S. Tafreshi, N. H. de Leeuw, A. Z. Moshfegh and O. V. Prezhdo, J. Phys. Chem. C, 2018, 122, 25606–25616.

52 E. Duverger, F. Picaud, L. Stauffer and P. Sonnet, J. Phys. Chem. A, 2016, 120, 9028–9041.

53 X. Ma, Y. Wu, Y. Lv and Y. Zhu, J. Phys. Chem. C, 2013, 117, 26029–26039.

54 E. S. Goh, J. W. Mah and T. L. Yoon, Comput. Mater. Sci., 2017, 138, 111–116.

55 Y. Lin and A. V. Akimov, J. Phys. Chem. A, 2016, 120, 9028–9041.

56 K. T. Chan, J. B. Neaton and M. L. Cohen, Phys. Rev. B: Condens. Matter Mater. Phys., 2008, 77, 235430.

57 B. Amin, S. Nazir and U. Schwingenschlo¨gl, Sci. Rep., 2013, 3, 1705.

58 K. J. Hamam and M. I. Alomari, Appl. Nanosci., 2017, 7, 261–268.

59 A. V. Akimov and O. V. Prezhdo, J. Am. Chem. Soc., 2014, 136, 1599–1608.

60 R. D. Senanayake, A. V. Akimov and C. M. Aikens, J. Phys. Chem. C, 2017, 121, 10653–10662.

61 M. E. Madjet, G. R. Berdiyorov, F. El-Mellouhi, F. H. Alharbi, A. V. Akimov and S. Kais, J. Phys. Chem. Lett., 2017, 8, 4439–4445.

62 E. Pradhan, R. J. Magyar and A. V. Akimov, Phys. Chem. Chem. Phys., 2016, 18, 32466–32476.

63 C. Murray, N. Dozova, J. G. McCaffrey, S. FitzGerald, N. Shafizadeh and C. Cre´pin, Phys. Chem. Chem. Phys., 2010, 12, 10406–10422.

64 Y. Kawashima and G. Katagiri, Phys. Rev. B: Condens. Matter Mater. Phys., 1995, 52, 10053–10059.

65 R. J. Nemanich and S. A. Solin, Phys. Rev. B: Condens. Matter Mater. Phys., 1979, 20, 392–401.

66 D. R. Tackley, G. Dent and W. Ewen Smith, Phys. Chem. Chem. Phys., 2001, 3, 1419–1426.